GEOPHYSICS, VOL. 78, NO. 2 (MARCH-APRIL 2013); P. 1–10, 13 FIGS.
10.1190/GEO2012-0241.1

Deep-water subsurface imagingusing OBS interferometry

Olivier Carrière[1] and Peter Gerstoft[1]

ABSTRACT

Seismic interferometry processing is applied to an active seismic survey collected on ocean bottom seismometers (OBS) deployed at 900-m water depth over a carbonate/hydrates mound in the Gulf of Mexico. Common midpoint processing and stacking of the extracted Green's function gives the subsurface PP reflectivity, with a horizontal resolution of half the receiver spacing. The obtained seismic section is comparable to classical upgoing/downgoing wavefield decomposition and deconvolution applied on a common receiver gather. Seismic interferometry does not require precise knowledge of source geometry or shooting times, but more accurate results are obtained when including this information for segmenting the signals before the crosscorrelations, especially when signals from distant surveys are present in the data. Reflectivity estimates can be obtained with the crosscorrelation of pressure or vertical particle velocity signals, but the pressure data gives the best resolution due to the wider frequency bandwidth and the reduced amount of noise bursts.

INTRODUCTION

The study and monitoring of complex natural marine hydrates require long-term or periodic data collection. For this purpose, data collected from long-term deployment of ocean-bottom seismometers (OBS) can be used for detecting and monitoring changes in hydrate distribution and other hydrocarbon related subsurface process. In this paper, empirical Green's functions are extracted from crosscorrelated signals collected over a 2D transect of OBS. Results are used to estimate seismic reflectivity of the shallow subsurface.

Data were acquired at Woolsey Mound, a very active carbonate/hydrates structure in Mississippi Canyon Lease Block 118 (MC118), Northern Gulf of Mexico, used as seafloor observatory by the Hydrates Research Consortium for more than a decade (McGee et al., 2009). The mound is about 1 km in diameter and located in nearly 900-m water depth. Recent study of the mound subsurface integrating several seismic data sets at different resolutions (backscatter, autonomous underwater vehicle [AUV], and shallow source/deep receiver [SSDR] surveys) has shown that the mound is formed by crestal normal faults nucleating at the top of a diapir-shaped salt body present in the shallow subsurface (Macelloni et al., 2012). The OBS transect used here crosses one of the main normal faults of the mound.

The measurement of pressure and particle velocity, as provided by multicomponent OBS, give access to the upgoing and downgoing wavefields (Schneider and Backus, 1964; Loewenthal et al., 1985; Amundsen and Reitan, 1995; Schalkwijk et al., 1999). In deep-water, when the target zone is within a few hundred meters of the seafloor, surface multiples arrive much later than primary reflections of interest, and the wavelet estimation follows directly from the upgoing/downgoing decomposition (Backus et al., 2006). Such a technique enables high-resolution images. As for other conventional seismic processing methods, this approach requires the knowledge of the shooting times and associated source-receiver geometry. Multicomponent acquisition gives also access to the shear reflectivity of the subsurface which is relevant for hydrates assessment (Backus et al., 2006).

As conjectured by Rickett and Claerbout (1999), and as demonstrated in many areas (helioseismology, ultrasounds, seismics, ocean acoustics, etc.) crosscorrelations of signals recorded on two distinct receivers enables the estimation of the Green's function between these two receivers, without knowledge of source position and wavelet. In seismics, Green's function extraction from crosscorrelations is referred to as "seismic interferometry" (Schuster, 2009). When applied to a controlled source survey, seismic interferometry is a redatuming process in which the redatum operator is deduced directly from the data, i.e., no velocity model is required, which is attractive when a complex structure overlies the targets (Bakulin and Calvert, 2006). Different crosscorrelation-based

Manuscript received by the Editor 26 June 2012; revised manuscript received 26 October 2012.
[1]University of California, Marine Physical Laboratory, Scripps Institution of Oceanography, San Diego, California, USA. E-mail: ocarriere@ucsd.edu; gerstoft@ucsd.edu.

methods exist and essentially differ in the weighting of the cross-correlations (Schuster and Zhou, 2006).

Seismic interferometry has become very popular since the 2000s with the mathematical proof of daylight imaging (Wapenaar et al., 2002; Schuster et al., 2004; Wapenaar, 2004). Many passive applications have been proposed, such as earthquake coda interferometry (Snieder et al., 2002; Shapiro and Campillo, 2004), surface-wave tomography (Shapiro et al., 2005; Gerstoft et al., 2006), body-waves interferometry (Roux et al., 2005; Miyazawa et al., 2008), or interferometric reflection seismics (Draganov et al., 2007). A special section of GEOPHYSICS edited by Wapenaar et al. (2006) draws up a comprehensive review of seismic interferometry history and applications. Wapenaar et al. (2010a) and Wapenaar et al. (2010b) give an updated review of seismic interferometry theory and its recent progresses.

The interest of active seismic interferometry for exploration has been demonstrated for vertical seismic profiling (Bakulin and Calvert, 2006; Vasconcelos et al., 2008), inverse vertical seismic profiling (Yu and Schuster, 2006), and crosswell data (Minato et al., 2011). A few papers also deal with OBS or OBC (ocean-bottom cable) data: Mehta et al. (2007) demonstrated the improvement of virtual source technique (Bakulin and Calvert, 2006) by decomposing the wavefield acquired on deep-water OBC data; elastic interferometry theory was proposed by Gaiser and Vasconcelos (2009) and applied on OBC data in shallow water for retrieving P-waves and P-to-S waves using refraction interferometry (Dong et al., 2006), Bharadwaj et al. (2012) generated supervirtual traces on OBS to increase signal-to-noise ratio (S/N) and facilitate the traveltime picking of far-offset traces and head waves. Haines (2011) applied interferometric processing to a deep-water OBS data set, using a large OBS array (160 elements spanning 4 km), for the purpose of shallow subsurface imaging (<500 m). However, the processing was restricted to single receiver interferometry (cross-correlation of different wavefields received on a single OBS) instead of crosscorrelating pairs of receivers. Here, deep-water OBS data are interferometrically redatumed followed by a model-based time-migration assuming horizontal layering and specular reflections. Signals are crosscorrelated between pairs of OBS and only PP reflections are considered. The obtained image is found to be comparable to a conventional image (using an upgoing/downgoing decomposition) from the same OBS data set but with a reduced horizontal resolution. In both methods, the processing is restricted to primary reflections. When applicable, the processing of surface multiples has been demonstrated to broaden illumination and increase horizontal resolution (Jiang et al., 2005; Dash et al., 2009). As horizontal propagation dominates ambient noise, the effective use of multiples has not been demonstrated yet in a purely passive approach. Moreover, the strong interferences from a distant seismic survey (see below) prevent here the use of multiples on many received shots.

With suitable noise field characteristics, the interferometric approach can be extended to ambient noise (or passive) processing. Passive monitoring typically requires longer acquisition time to accumulate sufficient energy along the stationary-phase paths and averaging down possible dominant but unwanted arrivals that bias the noise distribution. Given the increasing availability of receivers, this enables long-term passive seismic monitoring, thus suppressing the need for an active survey. Passive reflectivity imaging with OBC was proposed by Hohl and Mateeva (2006), but the results were not conclusive because of too short an observation time. At lower frequencies (0.35–1.75 Hz, the double-frequency microseismic band), de Ridder and Dellinger (2011) demonstrated passive interferometric imaging of Scholte-wave velocities using a few hours of data. Using local earthquakes, Minato et al. (2012) localize the oceanic crust surface using a 3D array of 28 OBS. Due to the localized nature of the sources, they propose to exclude receiver pair that do not correspond to stationary-phase paths to improve the imaging results. Harmon et al. (2007) and Yao et al. (2011) invert for shear-velocity structure in the crust and uppermost mantle using dispersion of Scholte-Rayleigh wave empirical Green's functions extracted from long-term (~1 year) recording on OBS. Interferometric processing at these low frequencies (0.01–1 Hz) requires large OBS offsets, typically tens or hundreds of kilometers. Low-frequency passive interferometry can also be useful for correcting the time drift of OBS, as proposed by Hatchell and Mehta (2010). In our case, only a single day of continuous passive monitoring was available from the April 2011 MC118 experiment. Unfortunately, distant seismic exploration dominates the noise sequence from a single direction and requires further processing before assessing the potential use of ambient noise for shallow subseafloor imaging. Therefore, we do not pursue interferometric imaging based on this passive data set and use the available active data set as a proxy for passive data processing.

The remainder of the paper is as follows: The next section details the OBS data set acquired at the Woolsey Mound and illustrates the principal reflectivity properties of the subsurface deduced from previous surveys. Then the OBS data from one of the endfire surveys are processed with a conventional upgoing/downgoing seismic processing. Next the same active data are processed using an interferometric approach. The same section then discusses how passive data would be interferometrically processed, compared to the present active interferometric processing.

OBS DATA

In April 2011, 15 OBS provided by Woods Hole Oceanographic Institution were deployed at the Woolsey Mound (Northern Gulf of Mexico) at 900-m water depth for a few days. The OBS were dropped from the sea surface and afterward the precise location was surveyed. These locations are used here. The OBS formed a line array with 11 OBS nominally spaced 25 m apart and 2 OBS spaced 500 m apart on each side, giving a total aperture of 2250 m (Figure 1). A gas-injection (GI) gun was towed near the surface above the OBS line, from south to north, shooting every 25 m covering 5500 m range. The active OBS survey was performed on April 7, from 10:01 to 11:03 UTC, resulting in a new shot every 10–15 s triggered manually due to computer failure. A crossfire active survey (west–east) and watergun shooting on the same day complete the data set but are not discussed.

The OBS signals can be combined through array processing to separate signals that have overlapping frequency content but originate from different azimuths, using a plane-wave beamforming processor (Van Veen and Buckley, 1988). Figure 2 shows the plane-wave beamformer output for the acoustic energy received at 30 Hz using the closely spaced OBS (OBS 1 to 11) around the period of the south-to-north survey. As the array is linear (1D), the beamformer output has an cylindrical symmetry around the array axis. Therefore, the resolved angle is usually termed "cone angle". When an acoustic source is at large range, this angle is the

azimuth. As revealed by the beamformer output, a distant seismic survey was present during the whole deployment at an azimuth of about 135° from north. The signals received from this survey perturb our data processing, especially at large source-receiver offset where signals from both surveys have similar amplitudes. They affect the deconvolution step in the upgoing/downgoing processing and create spurious arrivals in the interferometric approach.

The frequency content of recorded signals is below 100 Hz because the sampling rate was 5 ms. Signals are high-pass filtered (frequency cut-off 10 Hz) to remove low-frequency content from seismic activity that has insufficient resolution for closely spaced OBS. Traces are edited for spikes and noise bursts. Figure 3 illustrates the recording of a shot (number 51) on the hydrophone and the vertical geophone of each OBS. The strong arrival 0.15 s after the direct arrival is a bubble pulse and partially obscures the earliest PP reflection from the targets. The first water multiple is 1 s after the direct arrival. P-S reflections from the targets are hardly distinguished on isolated vertical geophone traces. They are more easily identified on common receiver gather representation for the vertical and horizontal geophones, from 0.6 s after the direct arrival. The average S/N is +21 dB on the hydrophones and +28 dB on the vertical geophone for small source offset (less than 500 m). However, the vertical geophones were more affected by noise bursts.

The OBS array passes over one of the main faults of the mound (Macelloni et al., 2012). No clear presence of bottom simulating reflectors (BSRs) was detected from previous surveys, but localized strong polarity-reversed reflection have been identified that might be generated by free gas (Macelloni et al., 2012). Such segmented reflector was also observed in another area of the Gulf of Mexico (Wood et al., 2008). Three-dimensional oil-industry data over the area covered by the OBS are shown in Figure 4. The dashed lines delimit the closely spaced OBS array on which the present work is focused. Reflection events are particularly discontinuous above the salt diapir.

CONVENTIONAL SEISMIC PROCESSING

In this section, OBS data are processed with an upgoing/downgoing decomposition to provide a benchmark reflectivity image for the purpose of comparison with the interferometric processing results. As formulated here, the upgoing/downgoing processing would not be applicable on a passive OBS data set, due to the unknown arrival angle (see "Application to OBS data").

The 4C sensors give access to the pressure component (hydrophone) and the three components of particle velocity (one vertical, two horizontals). These four components can be combined to estimate PP and PS reflections. Here, we focus on the PP reflections, following Backus et al. (2006). Above the seafloor, the pressure wavefield P is acoustically decomposed in the ray parameter (or horizontal slowness) frequency (p, ω) domain in its upgoing and downgoing parts, U and D, respectively, as (Amundsen and Reitan, 1995; Schalkwijk et al., 1999)

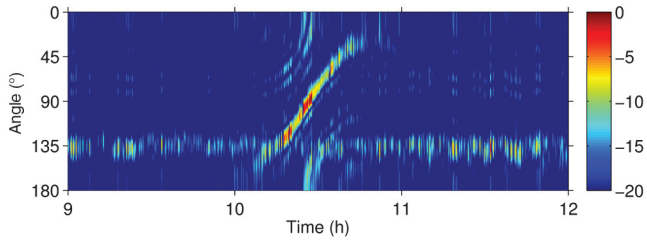

Figure 2. Plane-wave beamforming power output (dB) around the period of south-to-north active survey from 09:00 UTC. Angle is relative to north. The wave speed used in the beamforming is 1515 m/s. The "S"-shape (at 10:30) is our active survey (shot axis is on top of receiver axis). The nearly constant power at about 135° is from the distant seismic survey that lasted the whole deployment. This survey is at large offset so that the angle corresponds to azimuth.

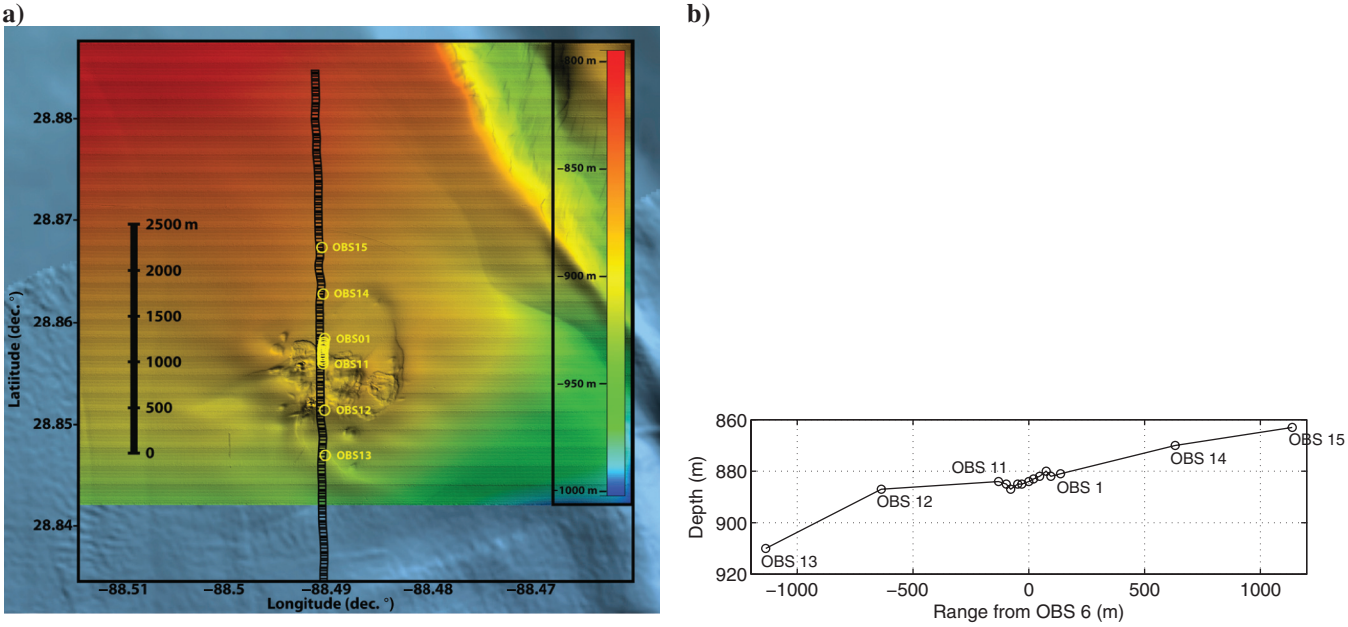

Figure 1. Gulf of Mexico, MC118 April 2011 experiment. (a) Acoustic source position during south-to-north active survey (black) and OBS positions (yellow). (b) OBS depths.

$$U(p,\omega,z) = \frac{1}{2}\left(P(p,\omega,z) - H^{\text{cal}}(\omega)\frac{\rho(z)}{q(z)}V_z(p,\omega,z)\right) \tag{1}$$

$$D(p,\omega,z) = \frac{1}{2}\left(P(p,\omega,z) + H^{\text{cal}}(\omega)\frac{\rho(z)}{q(z)}V_z(p,\omega,z)\right), \tag{2}$$

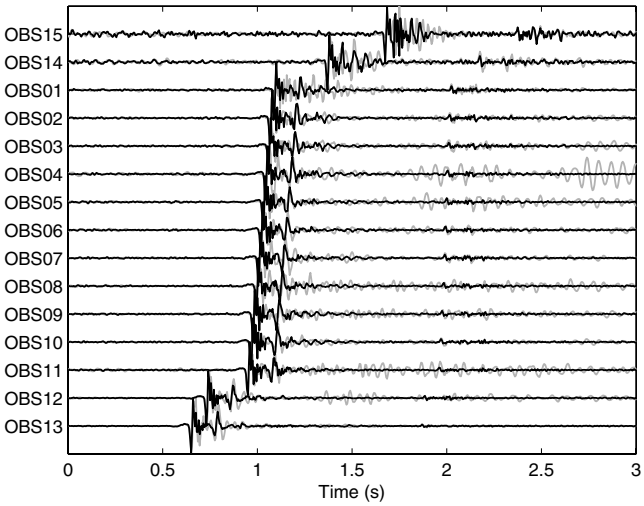

Figure 3. Shot number 51. Normalized pressure (black) and vertical particle velocity (gray) signals on the OBS elements during south-to-north active survey. The source is near vertical incidence for OBS 13. OBS 1–OBS 11 have 25-m spacing. OBS 12, 13, 14, and 15 are 500-m apart (see Figure 1).

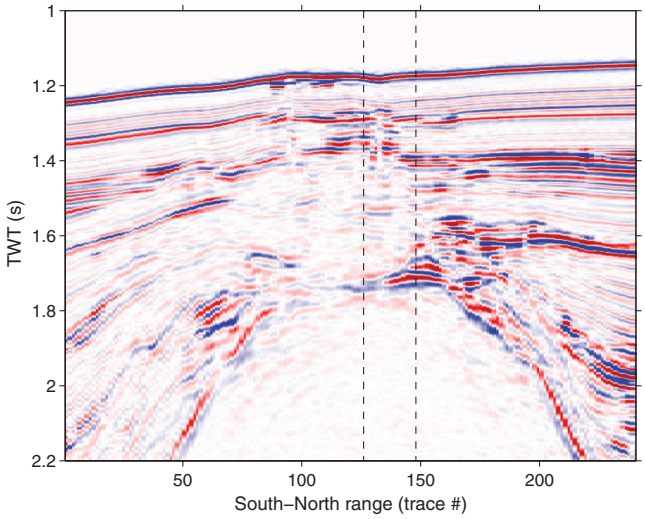

Figure 4. PP reflectivity estimated from proprietary deep seismic data, sea-level datum. The closely spaced OBS array position (OBS 1–OBS11, between the dashed lines) corresponds to the top of the salt dome. Inside this region, most of the reflections are discontinuous. A strong negative (blue) event is identified around 1.4 s (0.2 s below seabottom reflection). (Courtesy of WesternGeco).

where $P(p,\omega,z)$ and $V_z(p,\omega,z)$ are the pressure and the vertical particle velocity, $\rho(z)$ is the density, and $q(z)$ is the vertical ray parameter (or vertical slowness) defined by

$$q(z) = \sqrt{c(z)^{-2} - p^2}, \tag{3}$$

where $c(z)$ is the sound speed in water. The factor H^{cal} calibrates the vertical geophone to the hydrophone. Backus et al. (2007) demonstrated that a frequency-dependent sensor calibration was necessary only for the recovery of calibrated reflectivity in the shallow depths immediately below the seafloor (a few tens of meters) whereas constant gain factor provided accurate results for deeper reflections. Here, for each given OBS, a cross-equalization filter (Wiener filter) averaged over all traces provided an adequate calibration factor H^{cal} that enables satisfactory up/down separation. Nevertheless, no significant reflectivity difference was found between such a frequency-dependent calibration and a constant gain factor for the targets of interest (~200 m below the seafloor).

This decomposition is only valid just above the seafloor (no shear). Strictly speaking, the estimate of P- and S-wave components below the seafloor requires an elastic decomposition using P- and S-wave velocity and density below the receiver (Amundsen and Reitan, 1995; Schalkwijk et al., 1999). However, an acoustic decomposition is sufficient for imaging shallow subsurface PP and PS reflection events in deep-water (Backus et al., 2007).

Equation 2 is associated with the downgoing seismic wavelet. The PP reflectivity R is estimated from the spectral division of the upgoing wavefield U with the downgoing wavelet D (Loewenthal et al., 1985; Amundsen, 2001):

$$R = \frac{D^* U}{D^* D + \epsilon}, \tag{4}$$

where ϵ is a positive stabilization term and * denotes the conjugate. The reflectivity is related to the impedance contrast in the medium, and thus density and sound speed changes.

The deconvolution (equation 4) removes the source signature efficiently (wavelet and associated bubbles) and redatums the shots to the receiver datum on the seafloor. Surface multiples do not require a specific processing because they appear much later than the targeted events. The seafloor redatuming is important for the BSR detection, because the BSR tends to be parallel to the seafloor and therefore would appear as a straight-line event after redatuming. For the same reason, seafloor redatuming helps identify unconformities.

Equations 1–4 are applied independently to each common receiver gather (CRG). Figure 5a illustrates the resulting time-domain PP reflectivity for one receiver (OBS 3). Curved events are typically related to reflection events whereas horizontal events related to direct arrivals are removed by the deconvolution. The strong noise level on the resulting CRG is explained by signal corruption on the vertical geophone, but also due to another seismic exploration signals that perturb the upgoing/downgoing decomposition and deconvolution. The complex subsurface structure could explain discontinuities in the reflection curves.

The moveout is corrected using a ray-tracing model, assuming a four-layer subsurface model with a piecewise increasing P-wave velocity (1550, 1600, 1750, and 2000 m/s), with subsurface interfaces at depth 85, 150, and 470 m. This model gives the observed

two-way traveltimes (TWT) of 0.1, 0.2, and 0.55 s in the near-offset traces. The velocity range is similar to the P-wave velocity model obtained nearby by Murray and DeAngelo (2008), but does not consider any velocity drop that would be caused by free gas. The moveout correction reasonably flattens the reflection curves (see Figure 5b).

The geometry of acquisition (near-surface source, sea bottom receivers) makes the actual reflection points depth-dependent, even in a horizontally stratified environment. Therefore, the CRG data have to be converted to common depth point (CDP) gather. Theoretical curves of source-receiver offset versus time for reflection depth points at specified offsets from the receiver location are calculated using ray tracing (black lines in Figure 5b). CDP data are recovered by interpolation along these curves. Here, offset curves between $[-100, 100]$ m with a 5-m spacing are retrieved for each CRG, giving a 5-m horizontal resolution for the whole section. The CDP data are stacked to improve the S/N. The chosen offset of ± 100 m implies a minimum of five folds for the subseafloor section delimited by the OBS array and keeping a weak dependence to the velocity model. A maximum number of nine folds is achieved in the center of the array.

The upgoing/downgoing decomposition and deconvolution give a reasonable estimate of the PP reflectivity beneath the section covered by the closely spaced OBS, see Figure 6. Although the deconvolution operator is not optimal due to calibration issues, interferences from distant seismic exploration, and possible tilt of vertical geophones not accounted for (Li et al., 2004). Compared to the deep seismic data (Figure 4), the same three principal interfaces are well identified at 0.1, 0.2, and 0.55 s. The second reflector has a negative polarity, which might indicate the base of the hydrate stability zone (BHSZ). The third reflector most likely corresponds to the top of the salt dome identified in the deep seismic data acquired on a larger zone at the same location (Figure 4). This reflector is here continuous over the whole section whereas deep seismic data exhibit a discontinuity at the middle of the section. Overall, reflectors exhibit fewer discontinuities in OBS data. This difference might be reinforced by the datum difference (sea-level datum for the deep seismic data and seafloor datum for the OBS data) but is likely due to lack of horizontal resolution in the OBS data. No relevant reflections are detected below the third reflector (not shown).

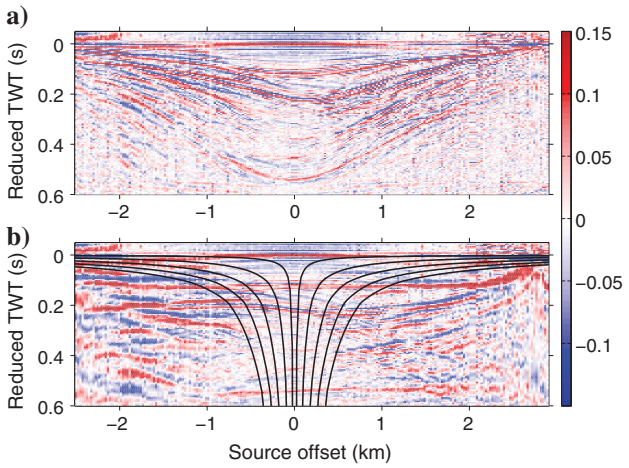

Figure 5. (a) Time-domain PP reflectivity estimate for OBS 3. (b) Moveout correction based on flat-layered earth model and an increasing P-wave velocity. The theoretical curves of source-receiver offset versus time for reflection depth points at receiver offsets ± 5 m, ± 25 m, ± 50 m, ± 75 m, and ± 100 m are shown (black lines).

GREEN'S FUNCTION EXTRACTION

Theory

Theoretically, the Green's function between two given points can be extracted by crosscorrelating waves recorded at these two points and excited by sources distributed on a closed surface around (see, e.g., Wapenaar, 2004). In the seismic community, Green's function extraction is better known as seismic interferometry. In most experimental configurations, receivers are typically not fully surrounded by sources and the latter are often located on a single side of the receiver pair. As demonstrated (Snieder et al., 2006; Brooks and Gerstoft, 2007), the lack of a closed surface for the source locations leads to artifacts in the reconstructed Green's function (spurious arrivals). This effect is reduced when the medium is sufficiently heterogenous (Wapenaar, 2006). For controlled sources (active data), a practical way to reduce spurious arrivals is isolating the direct arrival on one of the signals before crosscorrelation (Sheley and Schuster, 2003; Yu and Schuster, 2006; Mehta et al., 2007).

Considering a set of sources that are distributed over a horizontal line, the crosscorrelation of waves received on receivers A and B is given in the frequency domain by (Snieder et al., 2006)

$$C_{AB}(\omega) = |S(\omega)|^2 n \int G(r_A, r_s) G^*(r_B, r_s) dr_s, \qquad (5)$$

where $G(r_i, r_s)$ denotes the Green's function between receiver i at r_i and source at r_s, $S(\omega)$ is the source spectrum, and n is the number of sources per unit length. The integral in equation 5 gives the approximated Green's function $G(r_A, r_B)$ (Sabra et al., 2005; Snieder et al., 2006; Brooks and Gerstoft, 2007, 2009a).

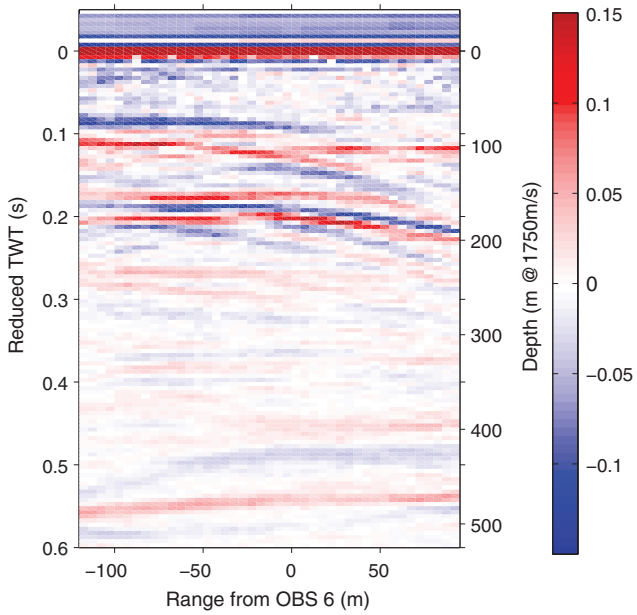

Figure 6. PP reflectivity obtained with conventional seismic processing (seafloor datum).

With the sources being distributed over a horizontal line, the exact phase dependence of the extracted Green's function is obtained through a Hilbert transform and a fractional derivative of C_{AB} (Snieder et al., 2006). Exact amplitude retrievals require reflection coefficients, path-dependent coefficients, and source spectrum terms, and are usually ignored. Therefore, the Green's function extraction from equation 5 enables the estimate of the reflector positions but cannot estimate their strength.

The active source is ~2 m below the sea surface and the towing trajectory roughly aligned to the receivers. Therefore, we only consider the stationary-phase points distributed along the receiver axis. Four kinds of contributing paths are distinguished, as illustrated in Figure 7. Type a is related to the direct arrival and involves no reflection. Type b involves first a reflection before reaching the receivers successively. Type c corresponds to a wave that encounters a reflection along the propagation between the two receivers. Type d exists for the multiple reflector case. Note that this type d does not correspond to a physical arrival between the receivers and would then be an artifact in the extracted Green's function.

Here, the receivers are considered at the same depth (see Figure 1b). The finite source offset makes that the stationary-phase point related to the direct arrival (type a) or reflected arrival (type b) is never reached, leaving only type c and d as precisely determined by the interferometric approach. Neglecting refraction, the source position giving stationary-phase path (type c) of a single specular reflection (assuming horizontal layering) is determined geometrically. Given a receiver spacing of r, water depth D, and reflector at depth H below the seafloor, the offset r_{st} of the stationary-phase point is (Figure 8)

$$r_{st} = \frac{rD}{2H}. \tag{6}$$

Therefore, considering a maximum source-receiver offset $r_{st} = 2500$ m, the minimum reflector depth resolved, H, increases linearly with receiver spacing r ($H \approx 5$ m with $r = 25$-m receiver spacing, $H \approx 50$ m with $r = 250$-m receiver spacing). This means that sensors separated by $r = 500$ m are not able to image a reflector located at less than $H = 100$ m below the seafloor.

On the other hand, a larger receiver spacing is expected to increase the accuracy of deep reflector localization (ignoring signal-to-noise ratio issues). Considering two reflectors at depths H and $H + \Delta h$, the source offset difference between their respective stationary-phase paths is (for $\Delta h \ll H$)

$$\Delta r = r_{st,H+\Delta h} - r_{st,H} = \frac{rD}{2(H+\Delta h)} - \frac{rD}{2H} \approx -\frac{rD}{2H^2}\Delta h. \tag{7}$$

The H^2 term is critical. Keeping shot spacing Δr (and water depth D) fixed, to maintain the same resolution Δh at a depth $H = 500$ m as at $H = 50$ m, requires the receiver spacing r to be increased by a factor $10^2 = 100$. With our limited array aperture of 250 m, the accuracy of reflector localization at 50-m depth with 25-m receiver spacing can only be maintained up to $50 \times \sqrt{10} \approx 150$-m depth, using the 250-m receiver spacing. For reflectors at 500-m depth, the present interferometric configuration can only localize them with an accuracy of 50 m. The inclusion of large offset OBS thus improves the accuracy of the deepest reflectors, but these cannot image the shallowest reflectors, given the limited source-receiver offset. To maintain the correspondence with upgoing/downgoing processing, the large offset OBS (OBS 12, 13, 14, and 15) were also discarded in the interferometric processing.

The strong bubble pulse that contaminates the signals (see Figure 3) would highly affect the crosscorrelations, resulting in a sum of shifted replica of the "true" crosscorrelation. With a bubble oscillation period of 0.1 s, the interferometric approach is thus not able to properly resolve the shallow subseafloor targets. Generally speaking, predictive deconvolution removes the tail of the wavelet (Bowen, 1986), although the very shallow reflections might be lost with such approach. Here, the traces are more efficiently deconvolved using the downgoing wavefield estimated from the seismic processing (equation 2). Practically, this downgoing wavefield is time-gated for containing only the direct arrival and the bubble pulse, resulting in an effective duration of 0.5 s. The deconvolution also flattens the spectrum over the processed band by taking the factor $|S(\omega)|^2$ of equation 5 into account and compensates for possible variations in the source wavelet.

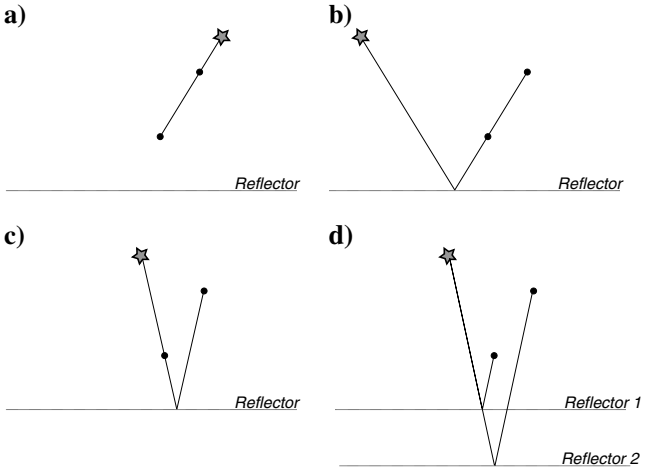

Figure 7. Stationary-phase paths contributing to the crosscorrelation. The order of the arrivals between the two receivers defines the sign of time lag in the crosscorrelation: Assuming the type (a) appears in the positive side, types (b) to (d) appear in the negative side. For type (b) and (c), the source positions that contribute to the opposite side of the crosscorrelation are easily deduced.

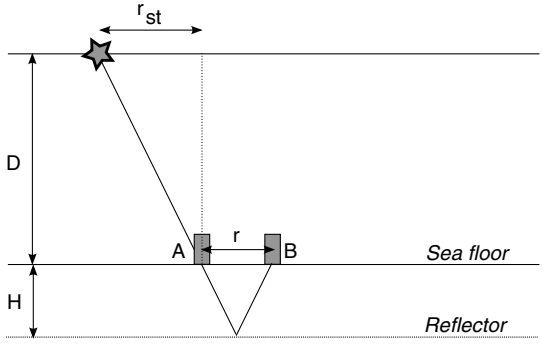

Figure 8. Two-dimensional geometric determination of the source position (star) giving a stationary-phase path of type c for the OBS pair A-B. Seafloor and reflector are assumed horizontal. The water depth is D and the reflector is at depth H below the seafloor.

Application to OBS data

Crosscorrelations (equation 5) are computed for pressure and vertical particle velocity signals. The actual survey shooting times are used for segmenting the received signals. The resulting segments (3-s duration) are then crosscorrelated between a receiver pair, so that each source offset gives a crosscorrelation (crosscorrelation gather). These crosscorrelations are summed to obtain the "total" crosscorrelation (left-hand term in equation 5). The band-limited (and amplitude-shaded) empirical Green's function are obtained after correcting the phase of the summed crosscorrelation. Figure 9 shows the crosscorrelation gather and associated summed crosscorrelation for OBS pair three through six, for pressure and vertical particle velocity signals. When crosscorrelating the vertical particle velocity, care must be taken to retrieve the correct polarity of the reflection event. Pressure and vertical particle velocity have a positive peak for the direct arrival, but exhibit opposite signs for primary reflection peaks.

Far-offset traces are typically noisier and might degrade the crosscorrelations. Given the maximum receiver spacing considered (250 m), and the maximum reflector depth (~500 m), crosscorrelations can be done on a reduced source offset, here 1000 m, without affecting the coverage of stationary-phase paths (type c in Figure 7). Due to the horizontal alignement of OBS, an infinite source offset is required to reach the stationary-phase paths of type a and b. The offset reduction thus affects the direct arrival position in the crosscorrelations, but the latter is not relevant for subsurface imaging. Tapering the crosscorrelations toward the extremal values of source offset reduces end-effects (Figure 9b and 9e).

Figure 9d exhibits PS wave arrivals around −0.8 s and +0.7 s. Primary PS waves propagate with a lower velocity than PP waves (shallow shear wave velocity is much lower than compressional wave velocity). Therefore, they can be distinguished from PP waves in the crosscorrelation gather (Figure 9d) by the late arrival time and flatter curvature of their related correlation peak trajectory (see Figure 10 for justification). The asymmetry between left and right PS waves peak trajectories is due to subsurface structure that is not perfectly horizontal as evident from CRG comparison or from the reflectivity image (Figure 6).

If the shooting times are unknown, the signals can be crosscorrelated using a sliding overlapping time window (Figure 11a). The use of actual shooting time reduces the effect of other sources; in

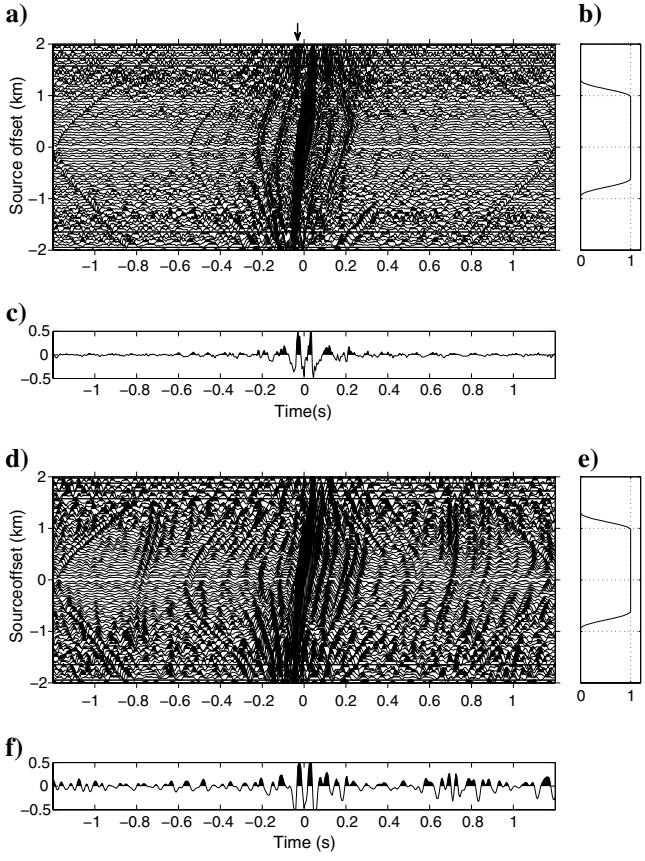

Figure 9. (a) Normalized crosscorrelation gather of pressure signals on OBS 6 and 3 (75-m spacing). The source offset is relative to OBS 6. Multiple-related crosscorrelation peaks appear partially at the far right and left as a negative (white) event due to the surface reflection. The strong peaks at −0.05 s at large positive source offset (arrow) are due to distant survey. (b) Taper applied for removing far-offset traces and reducing end-effects. (c) Summed crosscorrelations after tapering. The sum is normalized and clipped at 0.5. (d-f) Same as (a-c) for the vertical particle velocity.

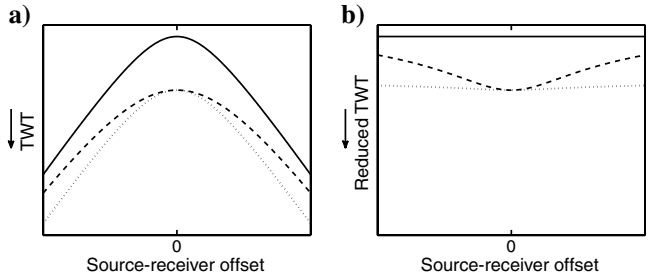

Figure 10. In a receiver gather (a), direct arrival (solid) and reflection events (dashed and dotted) are characterized by normal moveout. Here, the PP reflection (dashed) characterized by a higher average velocity than a PS reflection (dotted) has a flatter curvature. Velocities and depths of reflectors were chosen to have the same two-way traveltime at vertical incidence. In a correlation gather (b), the data are redatumed at the receiver level, so that direct arrival (solid) is flattened, and the PS reflection (dotted) characterized by a lower average velocity has a flatter curvature than the PP reflection (dashed).

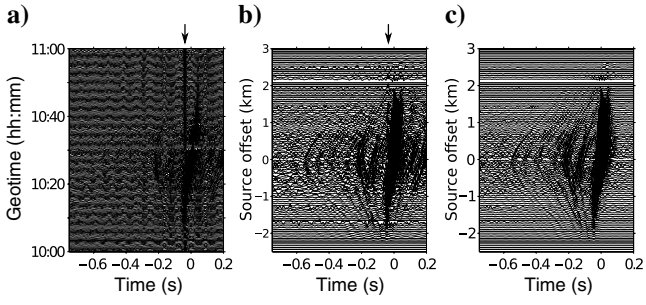

Figure 11. Crosscorrelation gather of pressure signals on OBS 6 and 3 (75-m spacing), (a) using sliding time window of 15 s with 66% overlap, (b) using the shooting times to segment the signals before crosscorrelation, (c) same as (b) with the additional isolation of direct arrival on one of the signals before crosscorrelation. The arrow on top of the figures indicates the position of the main crosscorrelation peak created by the distant seismic exploration. In (a), the vertical axis is geotime as source-receiver offset is not defined when exact shooting times are unknown.

particular, the strong interferences with distant seismic exploration. These interferences are still visible on some of the crosscorrelations (Figure 11b, arrow). They are further attenuated by keeping only the direct arrival (time gate) on one of the signals before crosscorrelation, as shown in Figure 11c. With such a time gate, events are traceable to larger source offsets in the crosscorrelation gather.

Figure 12 shows all empirical Green's functions extracted from pressure crosscorrelations based on shooting times and direct arrival isolation (as in Figure 11c). Peaks related to the direct arrivals are along a straight line. As expected from the horizontal alignment of the receivers, these peaks appear earlier than the theoretical direct arrival time delay. The coherent reflection hyperbolas in a common midpoint (CMP) gather are clearly seen. Note also that relative peak heights vary with receiver offset. Near OBS exhibit a large direct arrival and reduced reflections. As the OBS offset increases, the direct arrival is reduced and reflections are increased. This amplitude bias is due to the neglect of path-dependent terms between the exact Green's function and the computed crosscorrelation (Snieder et al., 2006; Brooks and Gerstoft, 2007) and is significant for the direct arrival peak for a horizontal array. To mitigate this effect, each summed crosscorrelation is renormalized by the energy after the direct arrival.

For a horizontally-layered subsurface, the redatuming that results from the interferometric processing associates each extracted Green's function to the CMP of the related OBS pair. Then an NMO correction based on the subsurface model is applied to obtain the equivalent zero-offset traces at the CMP. When pairs of receivers have similar CMP, their extracted Green's functions are stacked to improve the S/N. The resulting number of fold varies from one (boundaries of OBS array) to 10 (center of OBS array). This approach is a simplified crosscorrelation time-migration where trial points (scatterers) are located midway of the receiver pair and on parallels to the seafloor, only valid because of the nearly horizontal reflectors. For dipping reflectors, a full interferometric migration is needed (Schuster, 2009).

The resulting PP reflectivity estimates obtained with the pressure and vertical particle velocity signals are shown in Figure 13b and 13c. Peaks appearing at depths above 50 m are ignored because of the geometrical considerations between reflector depths and receiver spacing (equation 6). The three principal interfaces (0.1, 0.2, and 0.55 s) identified from the conventional seismic processing are seen on both crosscorrelation results (Figure 13, horizontal arrows). Event polarities are consistent. The amplitude of reflections are not comparable, due to the renormalization of the crosscorrelations and the ignored terms in the amplitude-shaded Green's functions (see, e.g., equation 13 in Brooks and Gerstoft (2007)), but relative amplitudes between reflection events are consistent. Most of the other reflection events identified in the conventional seismic processing are well retrieved with the interferometric processing, in particular with pressure signal crosscorrelations.

At reduced time 0, the apparent positive (vertical particle velocity) and negative (pressure) crosscorrelations are due to the limited source offset, resulting in biased direct arrival estimates, removed by the NMO correction (see Figure 12).

Vertical and horizontal resolutions are reduced compared to the conventional processing. The horizontal resolution of the interferometric processing is defined by half the receiver spacing. The vertical resolution is limited by the frequency band and the shot and receiver spacing (see equation 7). Crosscorrelation of the vertical geophone signals gives a somewhat deteriorated reflectivity image for two reasons: 1) Geophone signals have more noise bursts in our data set so that more segmented signals are muted at the trace edition step. This effect is reduced in the conventional seismic processing due to the combination of pressure and vertical particle velocity. 2) At higher frequencies (above 50 Hz), the geophone response is less than the hydrophones (not shown). In the conventional seismic processing, the calibration factor H^{cal} adjusted geophone response to hydrophone response, so that higher frequencies of the vertical particle velocity were amplified. Note that an upgoing/downgoing decomposition might be applied before interferometric processing to improve the results (Mehta et al., 2007). Here, such a step would also boost higher frequencies due to the calibration involved in the decomposition. However, the upgoing/downgoing decomposition relies on an obliquity factor correction (the angle of arrival). Although this correction can be neglected for small offsets (Mehta et al., 2007), the present

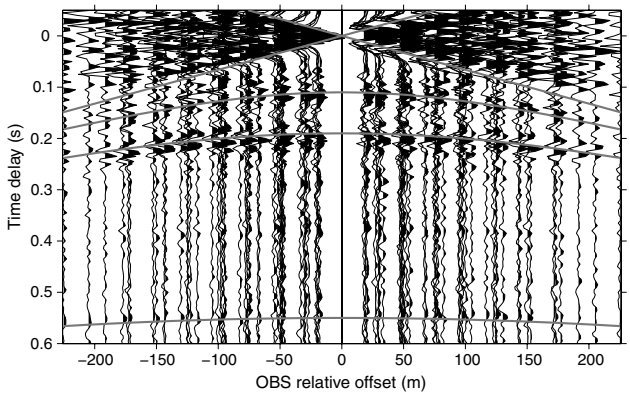

Figure 12. Empirical Green's functions from pressure signal crosscorrelations plotted versus the corresponding relative OBS offset. Autocorrelations (OBS offset = 0 m) are muted. The offset sign is positive for south-to-north-oriented pair. Simulated arrival times (gray) are obtained with ray tracing with the piecewise increasing velocity subsurface model with three reflectors. A linear time-variant gain is used.

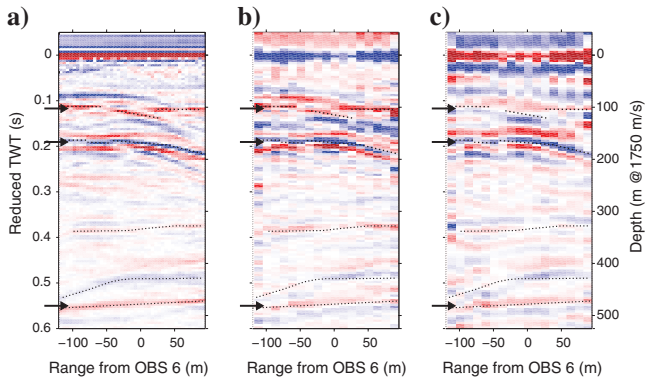

Figure 13. PP reflectivity obtained (a) with conventional seismic processing (repeated from Figure 6), and with stacked empirical Green's functions extracted from (b) pressure signal crosscorrelations and (c) vertical particle velocity signal crosscorrelations. For reference, several reflection events (dotted) and principal interfaces (→) identified with conventional seismic processing are shown.

upgoing/downgoing decomposition would not be applicable for purely ambient noise processing.

The seismic interferometry is more sensitive to the velocity model than the conventional seismic processing. The reason is that the time migration used in the latter (at the CRG to CDP conversion) is restricted to small depth-point offsets (up to 100 m, black lines in Figure 5) so that deeper velocities, typically more uncertain, have less impact on the reflectivity image. In the seismic interferometry, however, the entire velocity model is required for correcting the CMP gathers (Figure 12) on the full image range. This difference would be less if we were considering only near OBS in the interferometric approach or using larger depth-point offsets in the upgoing/downgoing seismic processing.

Implications for ambient noise seismic interferometry

It is not clear that passive seismic interferometry in the frequency range of active exploration (10–100 Hz) is realistic, because ocean waveguide horizontal noise might dominate. That was the case for the single day of passive data collected here, with a distant seismic exploration dominating the noise distribution from a single direction. This seismic exploration was also present during the active surveys; see the beamformer output in Figure 2.

In terms of processing, passive interferometry is essentially similar to active interferometry. The interferometric processing scheme used here would be the same if processing passive data, except that short-interval crosscorrelation would be based on a sliding overlapping time window instead of using the active survey shooting times (see Figure 11). Nevertheless, ambient noise interferometry requires different preprocessing steps, principally to better respect the assumptions required by interferometry theory (source spectrum correction, diffuse noise field, etc.), see, e.g., Bensen et al. (2007); Brooks and Gerstoft (2009b). On the other hand, the problem of bubble oscillations in active data is absent in ambient noise processing. Passive data might increase the vertical resolution due to a denser source distribution (smaller Δr in equation 7). Active data processing benefits from the isolation of direct arrival (see Figure 11c) which efficiently attenuates spurious arrivals.

Ambient noise survey requires long-term monitoring for reducing signals that bias the noise distribution. Here, the presence of another survey from a fixed location is an example where a longer term deployment would have been useful. As an alternative, using many sensors on a 2D or 3D grid would enable array processing techniques to filter unwanted signals.

CONCLUSION

The Green's function extraction from active OBS data is compared to conventional seismic processing based on upgoing/downgoing decomposition and deconvolution. Assuming a simple subsurface velocity model, both methods successfully localize the strong reflectors previously identified from oil-industry data. The interferometric processing reduces the horizontal resolution to half the sensor spacing whereas the standard seismic processing horizontal resolution is limited by the shot spacing. A higher resolution is obtained with the crosscorrelation of the pressure signals, the vertical particle velocity signals being characterized here by a lower frequency content.

Compared to the upgoing/downgoing decomposition scheme, the Green's function extraction does not require knowledge of source position. The short-interval crosscorrelation time windows can be defined independently from the shooting times. However, using the shooting times optimally frames the crosscorrelations and was found to reduce interferences from other acoustic sources. Interferences were further attenuated by isolating the direct arrival on one of the signals before crosscorrelation.

Active source signals are usually characterized by bubble pulses that affect the crosscorrelations. Here, the strong bubble pulse is efficiently removed by deconvolving the traces with the wavelet estimated from the upgoing/downgoing processing.

ACKNOWLEDGMENTS

The authors acknowledge Marco D'Emidio, University of Mississippi, for providing Figure 1a. Seismic data on Figure 4 were provided by WesternGeco. This work was supported by DOE NTEL, DOI BOEM, and DOC NOAA NIUST, via the Gulf of Mexico Hydrates Research Consortium, and by the NSF (EAR-0944109 and OCE-1030022).

REFERENCES

Amundsen, L., 2001, Elimination of free-surface related multiples without need of the source wavelet: Geophysics, **66**, 327–341, doi: 10.1190/1.1444912.

Amundsen, L., and A. Reitan, 1995, Decomposition of multicomponent seafloor data into upgoing and downgoing P- and S-waves: Geophysics, **60**, 563–572, doi: 10.1190/1.1443794.

Backus, M. M., P. E. Murray, and R. J. Graebner, 2007, OBC sensor response and calibrated reflectivity: 77th Annual International Meeting, SEG, Expanded Abstracts, 1044–1048.

Backus, M. M., P. E. Murray, B. A. Hardage, and R. J. Graebner, 2006, High-resolution multicomponent seismic imaging of deepwater gas-hydrate systems: The Leading Edge, **25**, 578–596, doi: 10.1190/1.2202662.

Bakulin, A., and R. Calvert, 2006, The virtual source method: Theory and case study: Geophysics, **71**, no. 4, SI139–SI150, doi: 10.1190/1.2216190.

Bensen, G. D., M. H. Ritzwoller, M. P. Barmin, A. L. Levshin, F. Lin, M. P. Moschetti, N. M. Shapiro, and Y. Yang, 2007, Processing seismic ambient noise data to obtain reliable broad-band surface wave dispersion measurements: Geophysical Journal International, **169**, 1239–1260, doi: 10.1111/gji.2007.169.issue-3.

Bharadwaj, P., G. T. Schuster, I. Mallinson, and W. Dai, 2012, Theory of supervirtual refraction interferometry: Geophysical Journal International, **188**, 263–273, doi: 10.1111/gji.2012.188.issue-1.

Bowen, A. N., 1986, A comparison of statistical and deterministic Wiener deconvolution of deep-tow seismic data: Geophysical Prospecting, **34**, 366–382, doi: 10.1111/gpr.1986.34.issue-3.

Brooks, L. A., and P. Gerstoft, 2007, Ocean acoustic interferometry: Journal of the Acoustical Society of America, **121**, 3377–3385, doi: 10.1121/1.2723650.

Brooks, L. A., and P. Gerstoft, 2009a, Green's function approximation from cross-correlation of active sources in the ocean: Journal of the Acoustical Society of America, **126**, 46–55, doi: 10.1121/1.3143143.

Brooks, L. A., and P. Gerstoft, 2009b, Green's function approximation from cross-correlations of 20–100 Hz noise during a tropical storm: Journal of the Acoustical Society of America, **125**, 723–34, doi: 10.1121/1.3056563.

Dash, R., G. Spence, R. Hyndman, S. Grion, Y. Wang, and S. Ronen, 2009, Wide-area imaging from OBS multiples: Geophysics, **74**, no. 6, Q41–Q47, doi: 10.1190/1.3223623.

de Ridder, S., and J. Dellinger, 2011, Ambient seismic noise eikonal tomography for near-surface imaging at Valhall: The Leading Edge, **30**, 506–512, doi: 10.1190/1.3589108.

Dong, S., J. Sheng, and G. T. Schuster, 2006, Theory and practice of refraction interferometry: 76th Annual International Meeting, SEG, Expanded Abstracts, 3021–3025.

Draganov, D., K. Wapenaar, W. Mulder, J. Singer, and A. Verdel, 2007, Retrieval of reflections from seismic background-noise measurements: Geophysical Research Letters, **34**, L04305, doi: 10.1029/2006GL028735.

Gaiser, J., and I. Vasconcelos, 2010, Elastic interferometry for ocean bottom cable data: Theory and examples: Geophysical Prospecting, **58**, 347–360, doi: 10.1111/(ISSN)1365-2478.

Gerstoft, P., K. G. Sabra, P. Roux, W. A. Kuperman, and M. C. Fehler, 2006, Green's functions extraction and surface-wave tomography from microseisms in southern California: Geophysics, **71**, no. 4, SI23–SI31, doi: 10.1190/1.2210607.

Haines, S. S., 2011, PP and PS interferometric images of near-seafloor sediments: 81st Annual International Meeting, SEG, Expanded Abstracts, 1288–1292.
Harmon, N., D. Forsyth, and S. Webb, 2007, Using ambient seismic noise to determine short-period phase velocities and shallow shear velocities in young oceanic lithosphere: Bulletin of the Seismological Society of America, **97**, 2009–2023, doi: 10.1785/0120070050.
Hatchell, P., and K. Mehta, 2010, Ocean-bottom seismic (OBS) timing drift correction using passive seismic data: 80th Annual International Meeting, SEG, Expanded Abstracts, 2054–2058.
Hohl, D., and A. Mateeva, 2006, Passive seismic reflectivity imaging with ocean-bottom cable data: 76th Annual International Meeting, SEG, Expanded Abstracts, 1560–1564.
Jiang, Z., J. Yu, G. T. Schuster, and B. E. Hornby, 2005, Migration of multiples: The Leading Edge, **24**, 315–318, doi: 10.1190/1.1895318.
Li, J., S. Jin, and S. Ronen, 2004, Data-driven tilt angle estimation of multicomponent receivers: 74th Annual International Meeting, SEG, Expanded Abstracts, **23**, 921–924.
Loewenthal, D., S. S. Lee, and G. H. F. Gardner, 1985, Deterministic estimation of a wavelet using impedance type technique: Geophysical Prospecting, **33**, 956–969, doi: 10.1111/gpr.1985.33.issue-7.
Macelloni, L., A. Simonetti, J. H. Knapp, C. C. Knapp, C. B. Lutken, and L. L. Lapham, 2012, Multiple resolution seismic imaging of a shallow hydrocarbon plumbing system, Woolsey Mound, Northern Gulf of Mexico: Marine and Petroleum Geology, **38**, 128–142, doi: 10.1016/j.marpetgeo.2012.06.010.
McGee, T., J. Woolsey, C. Lutken, L. Macelloni, L. Lapham, B. Battista, S. Caruso, and V. Goebel, 2009, A multidisciplinary sea-floor observatory in the Northern Gulf of Mexico: Results of preliminary studies: OCEANS 2009, MTS/IEEE Biloxi-Marine Technology for Our Future: Global and Local Challenges, 1–5.
Mehta, K., A. Bakulin, J. Sheiman, R. Calvert, and R. Snieder, 2007, Improving the virtual source method by wavefield separation: Geophysics, **72**, no. 4, V79–V86, doi: 10.1190/1.2733020.
Minato, S., T. Matsuoka, T. Tsuji, D. Draganov, J. Hunziker, and K. Wapenaar, 2011, Seismic interferometry using multidimensional deconvolution and crosscorrelation for crosswell seismic reflection data without borehole sources: Geophysics, **76**, no. 1, SA19–SA34, doi: 10.1190/1.3511357.
2 Minato, S., T. Tsuji, T. Matsuoka, and K. Obana, 2012, Crosscorrelation of earthquake data using stationary phase evaluation: insight into reflection structures of oceanic crust surface in the Nankai Trough: International Journal of Geophysics, **2012**, 1–8, doi: 10.1155/2012/101545.
Miyazawa, M., R. Snieder, and A. Venkataraman, 2008, Application of seismic interferometry to extract P- and S-wave propagation and observation of shear-wave splitting from noise data at Cold Lake, Alberta, Canada: Geophysics, **73**, no. 4, D35–D40, doi: 10.1190/1.2937172.
Murray, P., and M. DeAngelo, 2008, Simultaneous P-and S-wave interval velocity model building of near-seafloor geology using OBC data: 78th Annual International Meeting, SEG, Expanded Abstracts, 1038–1042.
Rickett, J., and J. Claerbout, 1999, Acoustic daylight imaging via spectral factorization: Helioseismology and reservoir monitoring: The Leading Edge, **18**, 957–960, doi: 10.1190/1.1438420.
Roux, P., K. G. Sabra, P. Gerstoft, W. A. Kuperman, and M. C. Fehler, 2005, P-waves from cross-correlation of seismic noise: Geophysical Research Letters, **32**, L19303, doi: 10.1029/2005GL023803.
Sabra, K. G., P. Roux, and W. A. Kuperman, 2005, Arrival-time structure of the time-averaged ambient noise cross-correlation function in an oceanic waveguide: Journal of the Acoustical Society of America, **117**, 164–174, doi: 10.1121/1.1835507.
3 Schalkwijk, K. M., C. P. A. Wapenaar, and D. J. Verschuur, 1999, Application of two-step decomposition to multicomponent ocean-bottom data: Theory and case study: Journal of Seismic Exploration, **8**, 261–278.
Schneider, W. A., and M. M. Backus, 1964, Ocean-bottom seismic measurements off the California coast: Journal of Geophysical Research, **69**, 1135–1143, doi: 10.1029/JZ069i006p01135.
Schuster, G. T., 2009, Seismic interferometry: Cambridge University Press.
Schuster, G. T., J. Yu, J. Sheng, and J. Rickett, 2004, Interferometric/daylight seismic imaging: Geophysical Journal International, **157**, 838–852, doi: 10.1111/gji.2004.157.issue-2.
Schuster, G. T., and M. Zhou, 2006, A theoretical overview of model-based and correlation-based redatuming methods: Geophysics, **71**, no. 4, SI103–SI110, doi: 10.1190/1.2208967.
Shapiro, N. M., and M. Campillo, 2004, Emergence of broadband Rayleigh waves from correlations of the ambient seismic noise: Geophysical Research Letters, **31**, L07614, doi: 10.1029/2004GL019491.
Shapiro, N. M., M. Campillo, L. Stehly, and M. H. Ritzwoller, 2005, High-resolution surface-wave tomography from ambient seismic noise: Science, **307**, 1615–1618, doi: 10.1126/science.1108339.
Sheley, D., and G. T. Schuster, 2003, Reduced time migration of transmission PS waves: Geophysics, **68**, 1695–1707, doi: 10.1190/1.1620643.
Snieder, R., A. Grêt, H. Douma, and J. Scales, 2002, Coda wave interferometry for estimating nonlinear behavior in seismic velocity: Science, **295**, 2253–2255, doi: 10.1126/science.1070015.
Snieder, R., K. Wapenaar, and K. Larner, 2006, Spurious multiples in seismic interferometry of primaries: Geophysics, **71**, no. 4, SI111–SI124, doi: 10.1190/1.2211507.
Van Veen, B. D., and K. M. Buckley, 1988, Beamforming: A versatile approach to spatial filtering: IEEE Transactions on Acoustics, Speech, and Signal Processing, **5**, 4–24.
Vasconcelos, I., R. Snieder, and B. Hornby, 2008, Imaging internal multiples from subsalt VSP data — Examples of target-oriented interferometry: Geophysics, **73**, no. 4, S157–S168, doi: 10.1190/1.2944168.
Wapenaar, K., 2004, Retrieving the elastodynamic Green's function of an arbitrary inhomogeneous medium by cross correlation: Physical Review Letters, **93**, 254301, doi: 10.1103/PhysRevLett.93.254301.
Wapenaar, K., 2006, Green's function retrieval by cross-correlation in case of one-sided illumination: Geophysical Research Letters, **33**, L19304, doi: 10.1029/2006GL027747.
Wapenaar, K., D. Draganov, and J. O. A. Robertsson, 2006, Seismic interferometry: History and present status: Geophysics, **71**, no. 4, SI1–SI4, doi: 10.1190/gpysa7.71.si1_1.
Wapenaar, K., D. Draganov, R. Snieder, X. Campman, and A. Verdel, 2010a, Tutorial on seismic interferometry: Part 1 — Basic principles and applications: Geophysics, **75**, no. 5, 75A195–75A209, doi: 10.1190/1.3457445.
Wapenaar, K., D. Draganov, and J. Thorbecke, 2002, Theory of acoustic daylight imaging revisited: 72nd Annual International Meeting, SEG, Expanded Abstracts, 2269–2272.
Wapenaar, K., E. Slob, R. Snieder, and A. Curtis, 2010b, Tutorial on seismic interferometry: Part 2 — Underlying theory and new advances: Geophysics, **75**, no. 5, 75A211–75A227, doi: 10.1190/1.3463440.
Wood, W. T., P. E. Hart, D. R. Hutchinson, N. Dutta, F. Snyder, R. B. Coffin, and J. F. Gettrust, 2008, Gas and gas hydrate distribution around seafloor seeps in Mississippi Canyon, Northern Gulf of Mexico, using multi-resolution seismic imagery: Marine and Petroleum Geology, **25**, 952–959, doi: 10.1016/j.marpetgeo.2008.01.015.
Yao, H., P. Gouédard, J. A. Collins, J. J. McGuire, and R. D. van der Hilst, 2011, Structure of young East Pacific Rise lithosphere from ambient noise correlation analysis of fundamental- and higher-mode Scholte-Rayleigh waves: Comptes Rendus Geoscience, **343**, 571–583, doi: 10.1016/j.crte.2011.04.004.
Yu, J., and G. T. Schuster, 2006, Crosscorrelogram migration of inverse vertical seismic profile data: Geophysics, **71**, no. 1, S1–S11, doi: 10.1190/1.2159056.

Queries

1. A check of online databases revealed a possible error in this reference. (Gaiser et al., 2010) The year has been changed from '2009' to '2010'. Please confirm this is correct.

2. A check of online databases revealed a possible error in this reference. (Minato et al., 2012) The page number has been changed from '101545' to '1-8'. Please confirm this is correct.

3. This query was generated by an automatic reference checking system. This reference (Schalkwijk et al., 1999) could not be located in the databases used by the system. While the reference may be correct, we ask that you check it so we can provide as many links to the referenced articles as possible.